PV Battery Charger Using an *L3C* Resonant Converter for Electric Vehicle Applications

Navid Shafiei, Martin Ordonez, *Member, IEEE*, Mohammad Ali Saket Tokaldani, *Student Member, IEEE*, and Seyed Ali Arefifar, *Senior Member, IEEE*

Abstract—In electric vehicles with rooftop PV panels, the solar irradiance and surface temperature can affect their performance and output voltages (e.g., $V_{pv} = 24$–45 V_{dc}). In these systems, the maximum energy must be extracted from the variable input voltage (PV panel), boosted by different gains, and stored in high-voltage battery packs. Furthermore, depending on the battery state of charge, the charger should operate in constant voltage, constant current, or constant power modes, all the way from complete discharge condition, up to the charged floating voltage phase ($V_{bat} = 230$–430 V_{dc}). This combination of the variable PV input voltage and different states of charge creates a significant regulation challenge for the converter. In this paper, a high-efficiency fourth-order *L3C* resonant converter is proposed with an extreme voltage regulation capability that can effectively extract the maximum power from the PV panels and respond to the battery states of charge at different voltage and current levels. The experimental results from a 350-W prototype prove the features of the proposed *L3C* resonant converter and demonstrate its ability to track the maximum input power while responding to the battery various states of charge.

Index Terms—Electric vehicle, full soft switching conditions, photovoltaic panel, wide dc–dc voltage regulation.

NOMENCLATURE

C_j	Diode junction capacitance (F).
$C_{w,s}$	Transformer winding capacitance (F).
f_0	Based resonant frequency (Hz).
f_s	Switching frequency (Hz).
G	Solar irradiation (kW/m^2).
$I_{L_{s_1}}$	First series resonant inductance current (A).
$I_{L_{s_2}}$	Second series resonant inductance current (A).
I_{out}	dc output current (A).
k	Boltzmann's constant ($k = 1.3806503 \times 10$ J/K).
L_{ext}	External series inductance (H).
$L_{lk,p}$	Transformer primary leakage inductance (H).
$L_{lk,s}$	Transformer secondary leakage inductance (H).
L_m	Transformer magnetizing inductance (H).

L_n	Resonant inductance ratio ($L_n = L_{s1}/L_p$).
L_p	Parallel resonant inductance (H).
L_s	Series resonant inductance ratio ($L_s = L_{s1}/L_{s2}$).
L_{s_1}	First series resonant inductance (H).
L_{s_2}	Second series resonant inductance (H).
n	Transformer turns ratio ($n = N_p/N_s$).
Q_L	Loaded quality factor.
q	Electronic charge ($q = 1.602 \times 10^{-19}$ C).
R_L	Load resistance (Ω).
T	Photovoltaic panel cell temperature (kelvin).
T_{amb}	Surface temperature (kelvin).
V_{AB_1}	1st harmonic of the full-bridge inverter.
V_{pv}	Solar PV panel voltage (V_{dc}).
V_{bat}	Battery voltage (V_{dc}).
Z_0	Based characteristic impedance (Ω).

I. INTRODUCTION

DC–DC power converters with variable voltage gain and boosting features are among the main components for PV energy systems, since the maximum power must be extracted from the low voltage, variable input source, and boosted to a high voltage level [1], [2]. In PV energy systems for electric vehicles (EVs) with rooftop PV panel, it is also essential to employ a rechargeable battery pack to store energy and release it later [3]–[7]. Using battery packs for energy storage imposes challenging design constraints for the power converter, due to different battery operating modes, including constant current, constant voltage, constant power, and no-load condition [8]. The combination of a PV panel and a rechargeable battery in an energy system requires extreme voltage gain variations from the input ($V_{pv} = 24$–45 V_{dc}) to the output ($V_{bat} = 230$–430 V_{dc}), and this needs to be supported by solar battery chargers. In this case, the charger should not only track the input voltage variation in order to extract the maximum available power from the PV panel, but also boost the input voltage according to the level of variable gain and respond to the battery different states of charge.

Recently, different studies have been dedicated to develop reliable and efficient nonisolated and isolated power converters for PV applications. Nonisolated power converter topologies which have been used in PV systems include boost converters, Cockcraft-Walton multipliers, coupled inductors, and switched inductors-capacitors with high-voltage gain capability as the dc–dc power conversion stage for PV to grid applications (boosts a low, variable input voltage of 30–50V_{dc}
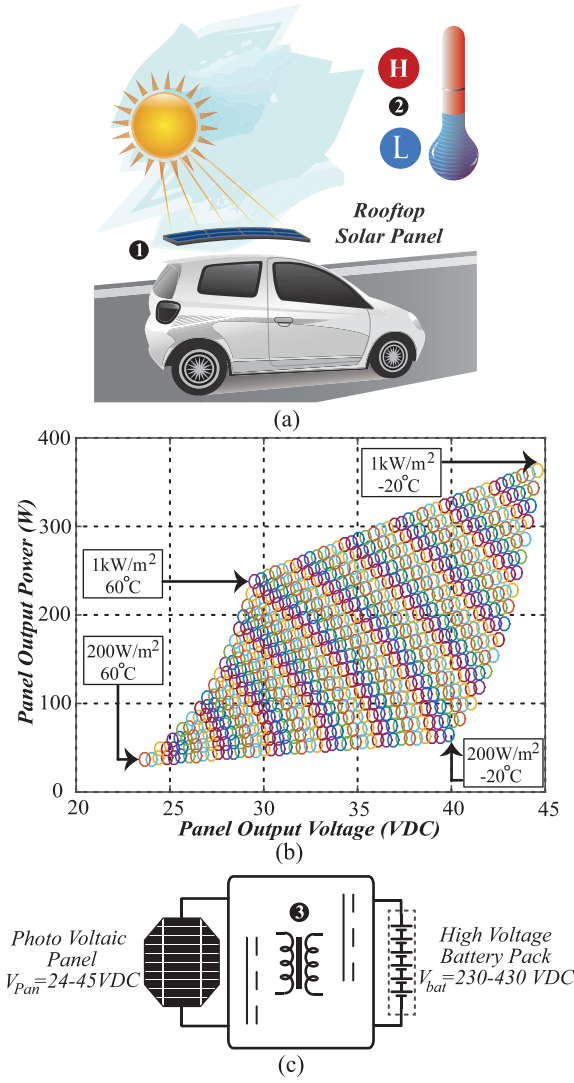
Fig. 1. (a) Example of EV with rooftop solar panel subject to changing sun irradiance ① and temperature ②. (b) PV panel power-voltage characteristic covered by the dc–dc converter. (c) Galvanic isolation ③ regulation requirement to supply 230–430 V_{dc} wide battery voltage from 24–45 V_{dc} PV voltage.

decrease the input current ripple and transfer the maximum input power to the output with soft switching across the main switches [19], [20]. These interesting converters target the maximum energy transfer from a variable input voltage to a fixed output voltage, rather than responding to different voltage and current operating modes of the high voltage battery pack. In particular, storage applications with new battery technologies (e.g., Li-Ion) push the charger output requirements of the PV converter to unprecedented levels. Insightful research on resonant converters has been presented in the literature with single and double conversion stages for battery charger or PV applications with fixed input and fixed output voltage, respectively; including current-fed parallel, modified and bidirectional, hybrid, and quasi-Z-source resonant converters [21]–[28]. These converters successfully handle the PV voltage variations and maximum power point tracking (MPPT) requirements or respond to different battery states of charge, but do not focus on both input and output variations at the same time. Resonant power converters will be reviewed in detail in Section III in order to present each topology configuration, its application, and the voltage regulation capability. The particular application, addressed in this paper, involves the challenging scenario of extracting the energy from a variable input voltage source (PV panel) and transferring it to a high-voltage battery pack, which needs to be regulated at different current and voltage levels. As an example, Fig. 1(a) shows a single PV panel on the rooftop of an EV. The power capacity range is from 50 to 350 W and the input voltage ranges widely from $V_{pv} = 24$–45 V_{dc}. This undesirable wide input variation is due to the effect of solar irradiance and surface temperature that affects the Power-Voltage characteristics of the PV panel illustrated in Fig. 1(b). As well, the battery pack depicted in Fig. 1(c) shows that the output voltage should comply with extreme regulation as well to cover 230–430 V_{dc}.

This paper proposes a high efficiency, isolated fourth-order *L3C* resonant converter with extreme regulation capability for PV to high-voltage battery pack applications with the aim of tracking the maximum input power while responding to the battery states of charge at different output voltage and current levels. In comparison with well-known resonant power converter topologies (e.g., *L3C2*, *LCLC*, *LCL2*, *LCC*, and *LCL*), the proposed topology presents a steep voltage gain versus frequency, means lower frequency variation for input–output regulation, which makes it a good candidate for PV to high-voltage battery pack applications. Also, the proposed resonant topology has a voltage gain of more than two for the resonant tank, which can be counted as a part of the boost action and reduces the transformer turns ratio and simplifies its structure. Due to its inherent over current capability, the proposed converter can control the charging current during constant current mode or transient conditions; this capability also eliminates the need for an over current and short-circuit protection, and facilitates the current control loop design. Due to operating in the inductive load region, power MOSFETs in the high-frequency *L3C* resonant converter always work in zero voltage switching for different load conditions, providing high-efficiency, low-noise output voltage. Moreover, the parallel resonant capacitor, put in the secondary of the

to a high, and fixed output voltage of 400 V_{dc}) [9]–[13]. Although nonisolated power converters can successfully boost the PV voltage and reach high performance, they are not recommended for EV applications that require mandatory galvanic isolation between the PV panel and the high voltage battery pack. According to safety standards *UL*60950 and *UL*1741, isolated applications require at least 4-kV galvanic isolation to be provided between the PV panel and the battery pack in order to prevent any high-voltage shock path [14], [15]. Among isolated PWM power converter topologies, flyback, current-fed push-pull topology, z-source, and phase shift-full-bridge power converters have attracted the most attention. These converters can achieve a high step-up gain from transformers with large turn ratios while tracking the input voltage variation by changing the effective duty cycle [16]–[18]. Different improvements such as interleaving and active clamp circuit have been presented in order to

transformer, leads to zero current switching (ZCS) of the output rectifier diodes, eliminates the voltage peak produced by the diodes reverse recovery current and decreases the noise in the output voltage. In this paper, the general equations for solar PV panels will be extracted and employed to determine the variation of power-voltage characteristics of a specific PV module versus irradiance and temperature variations. Then, a detailed review is presented for well-known resonant power converters in order to describe their structures and distinguish the difference between the proposed *L3C* resonant converter and its features in comparison with other resonant topologies. Later, the complete analysis of the *L3C* resonant converter with consideration of parasitic elements (including leakage inductances and parasitic capacitances) is obtained. Using the analytical equations extracted for fourth-order *L3C* resonant circuits, a 350-W dc-dc power converter is designed and implemented. Finally, experimental results are presented to demonstrate the circuit performance and to prove the extreme regulation feasibility for both input and output sides. The results show the *L3C* resonant converter can track all input voltage variations related to maximum input power [$V_{pv} = 24$–45 V_{dc} presented in Fig. 1(b)], while regulating the battery voltage from 230 to 430 V_{dc}.

II. Photovoltaic Module Characteristics as a Function of Irradiance and Temperature

As presented in Fig. 1(b), the PV panel maximum output power changes with respect to irradiance and temperature and the proposed *L3C* resonant converter should track these variations in order to transfer the maximum input power to the high-voltage battery pack [29]. In this section, the general equations for the solar PV panel will be extracted and employed to determine the variation of power-voltage characteristics of a specific PV module versus irradiance and temperature variations. A PV module consists of a number of interconnected solar cells forming a single unit. To model power-voltage characteristics of PV module, the power-voltage characteristics of a single solar cell should be determined and then expanded to obtain the behavior of a PV array or module. As shown in Fig. 2, a solar cell is traditionally represented by an equivalent circuit composed of a current source, an antiparallel diode, a series resistance (R_s), and a shunt resistance, R_p [30]. In Fig. 2, I_{rr} is the irradiance current, which is generated when the cell is exposed to sunlight and is dependent on the solar irradiance and surface temperature

The subscript *ref* represents the standard reference conditions and α_T represents the rate of change of the short-circuit current with respect to temperature and is usually provided by the manufacturers. The cell temperature is a function of changes in the surface temperature and changes in the isolation [30]

$$T = T_{amb} + \left(\frac{NOCT - 20°C}{0.8}\right) G. \qquad (1)$$

NOCT represents the Nominal Operating Cell Temperature provided by the manufacturer. In Fig. 2, I_D is the current of the antiparallel diode which characterizes the nonlinearity of the
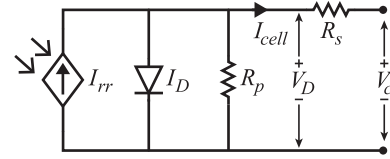

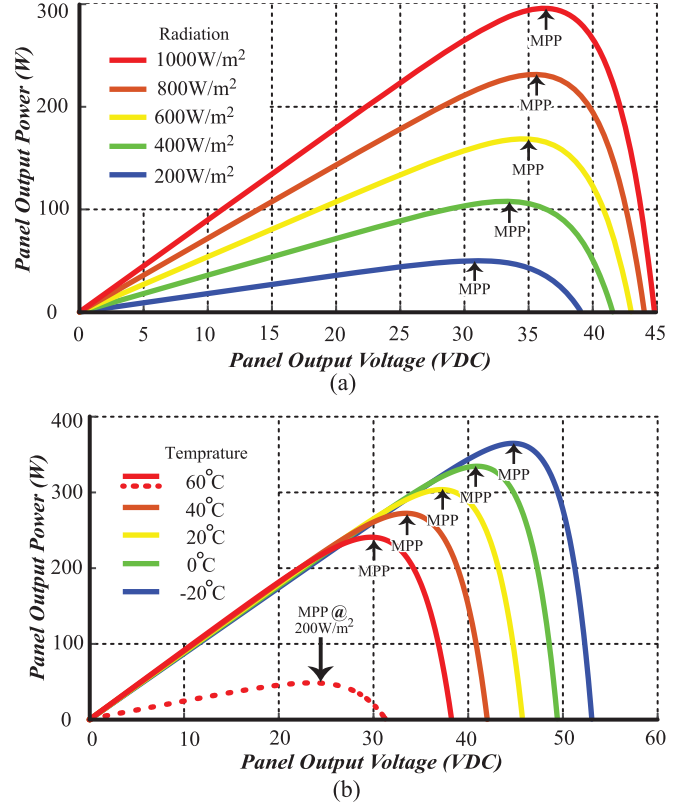Fig. 2. General model of a solar cell including parallel and series resistors.

Fig. 3. Variation of power-voltage characteristics of photovoltaic module as a function of (a) irradiance at 20 °C and (b) temperature at 1000 W/m². The dashed curve in (b) presents the minimum output power of the PV panel, occurs at maximum PV surface temperature (60 °C) and minimum sun irradiance (200 W/m²).

solar cell and is a function of diodes voltage and temperature, as presented in the following:

$$I_D = I_o\left(e^{\frac{qV_D}{nkT}} - 1\right). \qquad (2)$$

$$I_{rr} = I_{rr,ref}\left(\frac{G}{G_{ref}}\right)[1 + \alpha_T(T - T_{ref})]. \qquad (3)$$

In the recent equation, *n* is the ideality factor or the ideal constant of the diode and *T* is the temperature of the cell. The ideality factor (*n*) represents different mechanisms of moving carriers across the junction. If the transport process is purely diffusion, *n* will be 1 and if it is primarily recombination in the depletion region, *n* will be 2. As an example, for silicon, *n* will be 1.3 [31]. I_o is the diode saturation current or cell reverse saturation current

$$I_o = I_{o,ref}\left(\frac{T}{T_{ref}}\right)^3 e^{\left(\frac{qE_{g,ref}}{nkT_{ref}} - \frac{qE_g}{nkT}\right)}. \qquad (4)$$
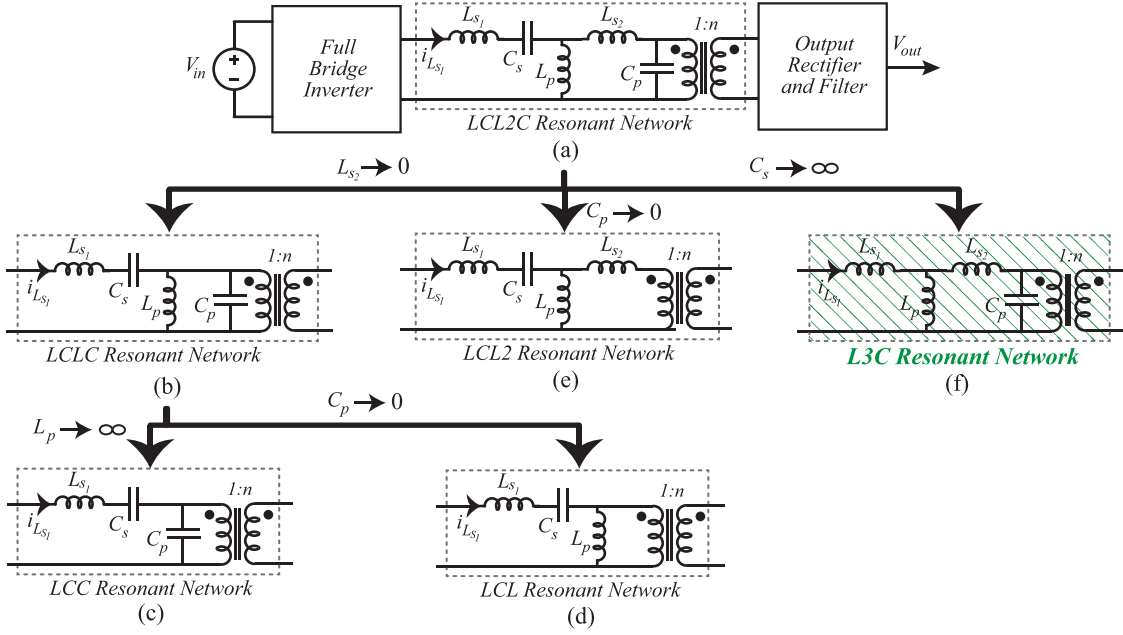
Fig. 4. Resonant power converters family. (a) Fifth-order $LCL2C$. (b) Fourth-order $LCLC$. (c) Third-order LCC. (d) Third-order LCL. (e) Fourth-order $LCL2$. (f) Proposed fourth-order $L3C$.

In the recent equation, E_g is the bandgap energy (eV) and depends on the materials used for manufacturing the cell. As an example, for silicon, this value can be calculated as follows [32]:

$$E_g = 1.16 - 7.02 \times 10^{-4} \left(\frac{T^2}{T + 1108} \right). \tag{5}$$

$I_{o,\text{ref}}$ is the reference diode saturation current and can be approximately obtained using the PV cells open circuit voltage (V_{oc}) and short-circuit current (I_{sc}) as presented in the following:

$$I_{o,\text{ref}} = \frac{I_{\text{sc}}}{e^{\frac{qV_{\text{oc}}}{nkN\text{OCT}}} - 1}. \tag{6}$$

Therefore, the relation between the voltage and current of the PV cell can be obtained as follows:

$$I_{\text{cell}} = I_{\text{rr}} - I_o \left(e^{\frac{q(V_{\text{cell}} + I_{\text{cell}} * R_s)}{nkT}} - \frac{V_{\text{cell}} + I_{\text{cell}} * R_s}{R_p} \right). \tag{7}$$

And finally, for a PV panel with N_s number of series cells and N_p number of parallel cells, (7) can be rewritten as follows:

$$I_{\text{cell}} = N_p I_{\text{rr}} - N_p I_o \left(e^{\frac{q(V_{\text{cell}} + I_{\text{cell}} N_s / N_p)}{nkT}} - 1 \right)$$
$$- \frac{V_{\text{cell}} + I_{\text{cell}} R_s N_s / N_p}{R_p N_s / N_p}. \tag{8}$$

The $V–I$ relationship of a PV panel presented in (8) can be used to obtain the power-voltage relationship of a PV panel in different surface temperature and solar irradiance and to determine the maximum power point of the PV panel. In this paper, the power-voltage characteristics of a PV module from Canadian Solar are presented in Fig. 1(b) [33]. For this specific example, the PV array consists of 72 PV cells connected in

series and parallel. The PV panel coefficients are extracted from the datasheet and by employing the recent equations, the variation of power voltage of photovoltaic module as a function of irradiance and temperature is presented in Fig. 3. The voltage related to the maximum power point for each condition is defined in Fig. 3, which indicates wide input voltage variation (V_{pv} = 24–45 V_{dc}). The input voltage derived in this section reflects the need for a dc–dc power converter with a wide input voltage regulation ability.

III. RESONANT POWER CONVERTERS REVIEW

Softly switched resonant converters are excellent candidates for dc–dc power supply design with wide regulation, due to their capability to produce variable voltage gains in different operating frequencies, while providing soft switching conditions for semiconductor devices [34]. In this section, well-known resonant power converters will be presented in order to review the application of each topology and distinguish the difference between the $L3C$ resonant circuit and other fourth-order ones. Also, this section will present and compare the voltage gain characteristics of each resonant power converter with the proposed $L3C$. To date, the most complicated resonant power converter contains a fifth-order resonant network, including three inductors and two capacitors, as presented in Fig. 4(a). The first application of $LCL2C$ resonant topology was for high-voltage dc–dc power supplies, due to its ability to absorb the parasitic capacitor of the transformer with a high turns ratio, also working with a fixed-frequency phase shift control approach [35]. Another interesting application of $LCL2C$ is for battery chargers, due to its capability to extend the switching frequency beyond the second resonant frequency and cover nearly all regions required in the battery VI plane [36]. While fifth-order $L3C2$ resonant converters can
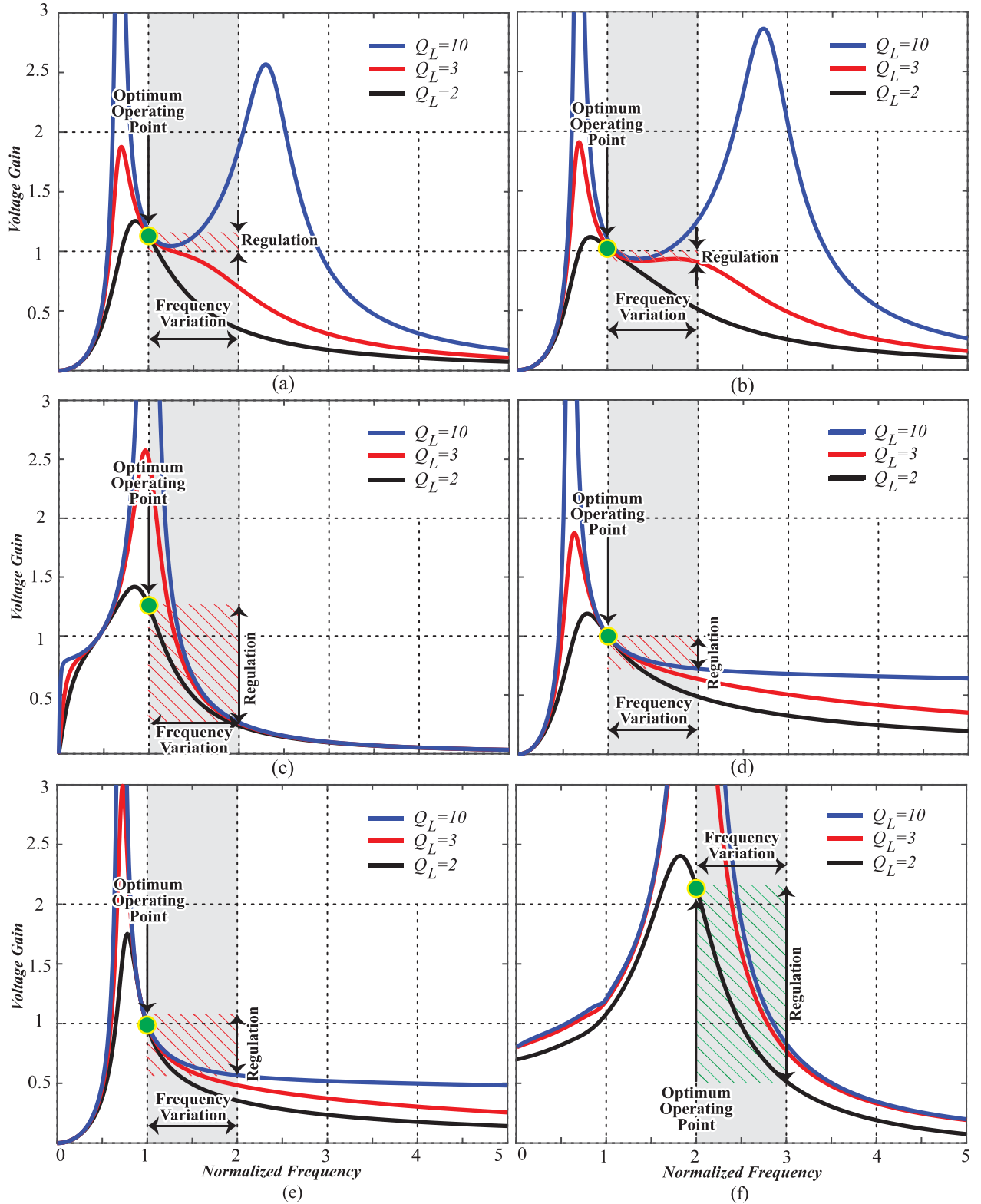
Fig. 5.   Voltage gains of different resonant power converters versus normalized switching frequency and constant values of normalized parameters (L_n, L_s, C_n, and Q_L). (a) $LCL2C$ for $L_n = 0.25$ and $L_s = 5$ and $C_n = 0.5$. (b) $LCLC$ for $L_n = 0.25$ and $C_n = 0.5$. (c) LCC for $C_n = 0.5$. (d) LCL for $L_n = 0.25$. (e) $LCL2$ for $L_n = 0.25$ and $L_s = 5$. (f) $L3C$ for $L_n = 0.25$ and $L_s = 5$.

regulate the output voltage, a wide switching frequency variation and nonoperating area leads to more complicated power and control circuit design. In comparison with fifth-order resonant topologies, the fourth-order $LCLC$ resonant converter does not take into account the effects of the transformer secondary leakage inductance ($L_{s_2} \rightarrow 0$), which leads to a less

accurate steady-state analysis and regulation capability [37]. This resonant circuit is presented in Fig. 4(b). Similar to the *LCL2C* resonant circuit, *LCLC* employs the parallel resonant capacitor in its circuit and can be used for high voltage dc–dc applications. Besides, *LCLC* has two resonant frequencies and is able to extend the switching frequency beyond the second resonant frequency for a better regulation. Both third-order *LCC* and *LCL* resonant converters are extracted from the *LCLC* resonant circuit, when $L_p \rightarrow \infty$ or $C_p \rightarrow 0$, respectively. These two third-order resonant power converters have been reported in the literature for a variety of applications. The *LCC* resonant converter has been employed in dc–dc power converters with low-voltage and high-voltage output level [38], [39]. As shown in Fig.4(a)–(f), this resonant converter has a relatively better regulation capability in comparison with other well-known resonant converters. Even though the *LCL* resonant topology has become a popular resonant converter for battery charger and telecom applications, it is well understood that the existence of diode junction capacitances creates limitations for *LLC* resonant converter in terms of the maximum operating frequency and regulating the input–output voltage in a wide range [8], [40], [41]. In dc–dc power converters with a low output voltage, the transformer parasitic capacitor can be neglected and in Fig. 4(a) with $C_p \rightarrow 0$, a higher order model for *LCL* resonant circuit can be obtained. In fact, the *LCL2* resonant converter employs third-order model of the transformer, which leads to a more accurate steady-state analysis. The research in [42] has proved that the *LCL2* resonant converter has steeper voltage gain curves and wider output voltage regulation in comparison with the *LCL* resonant power converter. Although all of the above-mentioned resonant topologies can to some extent respond to the input voltage variation and operate under MPP, they struggle to attain the required output voltage regulation, which makes them unsuitable for the target application.

The proposed resonant topology presented in this paper can be obtained by removing the series resonant capacitor in Fig. 4(a), $C_s \rightarrow \infty$. It means that the fourth-order *L3C* can be obtained from the fifth-order *LCL2C* resonant topology if the series resonant capacitor is selected as a dc blocking capacitor or completely eliminated from the circuit. Studying the behavior of the *L3C* resonant circuit presented in Fig. 4(f) shows that this topology presents a completely different behavior for the voltage gain versus frequency. In order to compare the regulation capability of the previous resonant power converters and with the proposed one, normalized steady-state equations of each resonant topology are used to draw voltage gains versus normalized frequency. Fig. 5 presents resonant converters voltage gains for the same amount of normalized parameters and loaded quality factor Q_L. For each resonant converter, the normalized frequency variation is selected to be one and the voltage regulation characteristic is studied. According to the obtained results, *L3C* and *LCLC* resonant topologies have the highest and lowest regulation capability among all resonant power converters. In comparison with the resonant converters presented in Fig. 4(a)–(e), the proposed topology presents a steep voltage gain versus frequency, meaning lower frequency variation for input–output regulation.
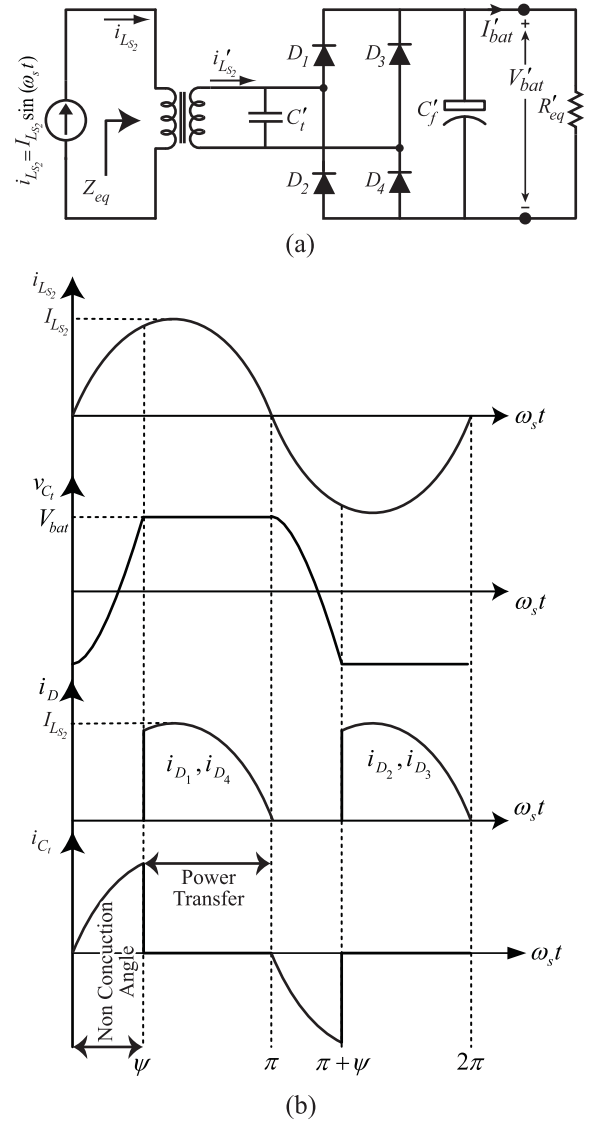

Fig. 6. (a) Output rectifier with the parallel resonant capacitor. (b) Main waveforms.

More importantly, all the well-known resonant converters present a voltage gain of around one for the optimum operating point, while the proposed *L3C* topology has a voltage gain of more than two, which makes it an excellent candidate for PV to high-voltage battery pack applications.

Another important advantage of resonant topologies with a parallel resonant capacitor, including *LCL2C*, *LCLC*, *LLC*, and *L3C* is the ability to provide soft switching conditions for output rectifier in all operating conditions. Fig. 6 shows the schematic of the output rectifier with the parallel resonant capacitor along with its main waveforms. According to Fig. 6, there are two intervals in each switching period that the output rectifier diodes turn off and the resonant circuit is being disconnected from the load, called nonconduction angle. This off-state interval leads to ZCS of the diodes and eliminates the noise in the output voltage that is produced by the diodes reverse recovery current [35]. Also, due to the semisinusoidal waveform of the diode voltage, the diodes turn on and off at
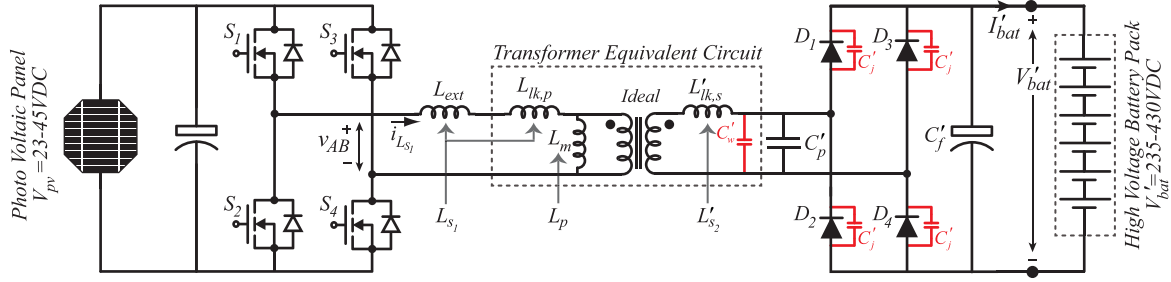
Fig. 7. Full-bridge $L3C$ resonant converter schematic with capacitive output filter, applicable for PV to high-voltage battery applications.

low (dv/dt) and the drawback effect of the diode junction capacitance during transient times can be minimized. Once the voltage across the parallel resonant capacitor reaches to the output voltage, the rectifier diodes are forward biased and start transferring power to the load. Despite resonant topologies with a parallel resonant capacitor, LCL and $LCL2$ resonant topologies can only provide soft switching condition for output rectifier diodes when the converter operates at or below short-circuit resonant frequency [42], [43].

IV. STEADY-STATE ANALYSIS OF $L3C$ RESONANT CONVERTER

Fig. 7 shows a complete schematic of the proposed $L3C$ resonant converter, including transformer secondary side and diode junction parasitic capacitances. In Fig. 7, a fourth-order model of the transformer has been employed as a model for the nonideal transformer [44]. In the proposed resonant converter, the parallel resonant capacitor in the secondary side of the transformer can merge all parasitic capacitors of the secondary side into the resonant circuit. According to Fig. 7, the proposed topology does not employ any series resonant capacitor in the primary side of the converter, which eliminates the dielectric power loss and facilitates the charger design in terms of component selection. In Fig. 7, all of the elements in the secondary side are defined with an apostrophe, but in all equations, the variables and elements are transferred to the primary side with respect to the transformer turn-ratio, and are shown without an apostrophe. According to Fig. 7, the total amount of parallel capacitance in the secondary of the transformer can be obtained as follows [45]:

$$C_t = C_p + C_{w,s} + C_j. \tag{9}$$

In order to model the interaction between the output side (the output rectifier, output filter, and load) and the parallel resonant capacitor, the output-side and parallel resonant elements are modeled using an equivalent impedance. The elements of the equivalent circuit are defined as follows [37]:

$$R_{eq} = \frac{\sin^2 \psi}{\pi C_t \omega_s}, \quad C_{eq} = \frac{\pi C_t}{\psi - \sin \psi \cos \psi}. \tag{10}$$

The angle ψ is the interval during which the output rectifier diodes turn off and the resonant circuit is disconnected from the load (presented in Fig. 6) and is given by:

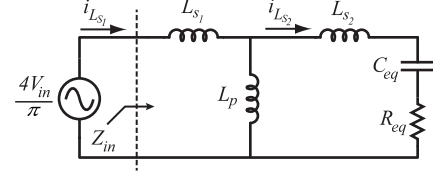$$\psi = \cos^{-1}\left(\frac{\pi - 2\omega_s R_L C_t}{\pi + 2\omega_s R_L C_t}\right). \tag{11}$$

Fig. 8. AC equivalent circuit of the $L3C$ resonant converter.

Fig. 8 shows the ac equivalent circuit of the resonant circuit along with the equivalent impedance of the transformer secondary side. By using this equivalent circuit, it is possible to employ the first harmonic approximation technique for analysis of the $L3C$ resonant circuit. In order to calculate the output current, the second series resonant inductor current is considered purely sinusoidal. Due to the nonconduction angle of the output rectifier, the output current and output voltage can be obtained as follows:

$$I_o = \frac{1}{2\pi}\left(\int_\psi^\pi i_{L_{s_2}} d(\omega_s t) + \int_{\pi+\psi}^{2\pi} i_{L_{s_2}} d(\omega_s t)\right)$$
$$= \frac{(1 + \cos \psi)}{\pi} I_{L_{s_2}} \tag{12}$$

$$V_{out} = R_L . I_{out} = R_L \frac{(1 + \cos \psi)}{\pi} I_{L_{s_2}}. \tag{13}$$

According to Fig. 8, applying KVL and KCL gives the relation between output voltage and resonant circuit input current

$$I_{L_{s_2}} = \left| \frac{j\omega_s L_p}{j\omega_s L_p + j\omega_s L_{s2} + R_{eq} + \frac{1}{j\omega_s C_{eq}}} \right| I_{L_{s_1}}. \tag{14}$$

In order to calculate the resonant circuit input current, the input impedance of the ac equivalent circuit should be obtained, which can be expressed by

$$\mathbf{Z_{in}}(j\omega_s) = j\omega_s L_{s_1} + (j\omega_s L_p) || \left(j\omega_s L_{s_2} + R_{eq} + \frac{1}{j\omega_s C_{eq}}\right). \tag{15}$$

One of the advantages of the proposed resonant converter is its ability to limit the output current. In this case, the $L3C$ resonant converter can not only provide a constant current for charging the battery pack, but also protect the full-bridge inverter from over current and short-circuit conditions. In over-current conditions, $R_{eq} \to 0$ and by considering (15), Z_{in}
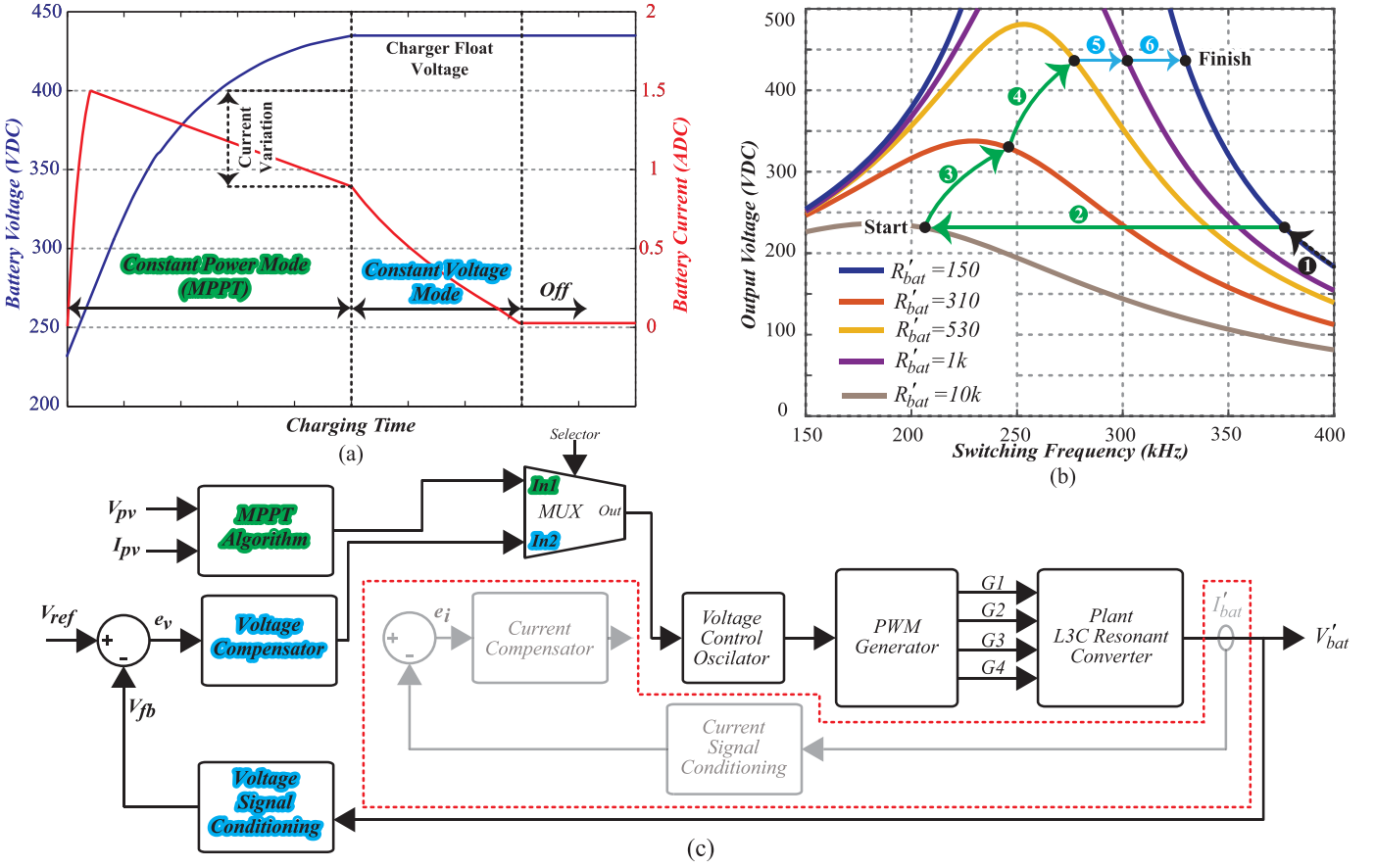
Fig. 9. (a) Charging cycle profile for a high-voltage battery pack by considering the constant power mode (MPPT) for the PV panel and constant voltage mode during the charger float voltage. (b) *L3C* battery charger trajectory for different states of charge. (c) *L3C* control loop block diagram for PV to battery applications. Due to the inherent current limit capability of the *L3C* resonant power converter, the current control loop (blocks inside the dashed red line) is eliminated from the control scheme.

would be as follows:

$$\mathbf{Z_{in}}(j\omega_s) = j\omega_s L_{s_1} + j\omega_s L_p || j\omega_s L_{s_2}. \tag{16}$$

In this case, the inverter switches are loaded by an inductor that can limit the switches current and also load current. In fact, the resonant circuit provides an inherent short-circuit protection at any operating frequency for the full-bridge inverter. In the ac equivalent circuit, the fundamental component of the resonant circuit input voltage ($v_{AB_1}(t)$) can be obtained as follows:

$$v_{AB_1} = \frac{4V_{in}}{\pi}\sin(\omega_s t). \tag{17}$$

According to Fig. 8 and (15) and (17), the amplitude of $I_{L_{s1}}$ (MOSFETs current) can be obtained as follows:

$$I_{L_{s1}} = \frac{4V_{in}}{\pi|\mathbf{Z_{in}}(j\omega_s)|}. \tag{18}$$

The following normalized parameters are introduced for the resonant circuit:

$$L = L_p + L_{s_2}, \quad L_n = \frac{L_{s_1}}{L_p}, \quad L_s = \frac{L_{s_1}}{L_{s_2}}$$

$$Z_0 = \sqrt{\frac{L}{C_t}}, \quad Q_L = \frac{R_L}{Z_0}, \quad \omega_0 = \frac{1}{\sqrt{LC_t}}, \quad \omega_n = \frac{\omega_s}{\omega_0}. \tag{19}$$

Considering (13), (14), (18), and (19), the normalized voltage gain of the *L3C* resonant converter is obtained as follows:

$$M_v = \frac{V_{out}}{V_{in}} = \frac{Q_L Z_0 (1 + \cos\psi)}{\pi V_{in}}$$

$$\cdot \left| \frac{\frac{j\omega_n L_s}{L_n + L_s}}{\frac{\sin^2\psi}{\pi\omega_n} + j\left(\frac{\omega_n L_s}{L_n + L_s} + \frac{\omega_n L_n}{L_n + L_s} - \frac{\psi - \sin\psi\cos\psi}{\pi\omega_n}\right)} \right|$$

$$\times \frac{4}{\pi\left|\mathbf{Z_{in,n}}(j\omega_n)\right|}$$

$$\psi = \cos^{-1}\left(\frac{\pi - 2\omega_0 Q_L}{\pi + 2\omega_0 Q_L}\right). \tag{20}$$

In Section VI, (20) will be employed to study the voltage gain behavior of *L3C* resonant converter and circuit elements design.

V. *L3C* CONTROL STRATEGY FOR PV TO BATTERY APPLICATIONS

In this section, the control block diagram of the *L3C* resonant converter as a charger for PV to high-voltage battery pack will be explained. A Li-Ion battery pack has two different modes in its charging profile, which are constant current and constant voltage modes, and EV on-board battery chargers

are designed based on this battery charging profile [46], [47]. During the constant current mode, the battery pack is charged with the maximum allowable charging current until the battery voltage reaches the float voltage. In the constant voltage mode, the battery voltage is regulated at the float voltage ($V'_{\text{bat}} =$ 430 V) and the charging action continues until the charging current drops to a certain amount of the rated current (e.g., 3%). The power level of the on-board battery charger for EV applications is around 3 kW, and depending on the battery pack capacity, the charger can provide 10 to 20 A during constant current mode [47], [48]. However, the maximum PV panel power is limited to several hundred watts, which means the charging current is much lower than on-board chargers. Although a maximum charging current is allowed for the Li-Ion battery pack, it is also possible to charge the battery at a lower rate with a longer charging time without reducing the life [49]. Fig. 9(a) presents the charging cycle profile of the high-voltage battery pack when the maximum input power is available by the PV panel [$P_{\text{pv}} = 365W$ at $V_{\text{pv}} = 44.5$ V_{dc} according to Fig. 3(b)] and the battery voltage dropped to its minimum level ($V'_{\text{bat}} = 230$ V_{dc}). Since the target for the PV to the battery application is to extract the maximum power from the input, the charging profile can be divided into two main parts, which are constant power mode (MPPT) and constant voltage mode. Considering the input power (P_{pv}) equal to 365 W and an average efficiency of 96% for the resonant power converter, the transferred power to the battery by the resonant converter will be 350 W. During the first stage of the charge, the battery voltage increases from its minimum level to the charge float voltage and the output power is constant; therefore, the charging current slowly decreases from 1.5 to 0.8 A, as shown in Fig. 9(a). In the second stage, the battery voltage is regulated at the float voltage until the battery is fully charged. Fig. 9(b) shows operating trajectories of the $L3C$ resonant converter during different states of charge. The details of each trajectory are presented as follows.

①: The starting switching frequency of the $L3C$ resonant converter is set to be the maximum value. Starting from $f_s = 400$ kHz, the output voltage is less than 230 V_{dc}, and the converter works under no-load condition. In this case, the controller decreases the switching frequency until the output voltage reaches the battery voltage ($V'_{\text{bat}} = 230$ V_{dc}).

②: When the output voltage reaches to 230 V_{dc}, the battery pack starts to sink the charging current. At this stage, the MPPT algorithm kicks in and, by decreasing the switching frequency, the maximum power is extracted from the PV panel. Finally, the operating point of the converter will be settled in $V'_{\text{bat}} = 230$ V_{dc} and $I'_{\text{bat}} = 1.5$ A_{dc}.

③ and ④: According to Fig. 9(a), during each state of charge the battery pack has different voltage and current levels, and therefore behaves similar to a variable resistor. Starting from $V'_{\text{bat}} = 230$ V_{dc} to $V'_{\text{bat}} = 430$ V_{dc}, Fig. 9(b) presents three voltage gain curves of the $L3C$ resonant converter when the maximum power is transferred to the battery pack (gray, red, and yellow curves). During these states, the MPPT algorithm is looking for maximum power from the PV panel and adjusts the switching frequency accordingly. In this stage, the charging current decreases from 1.5 to 0.8 A_{dc}.
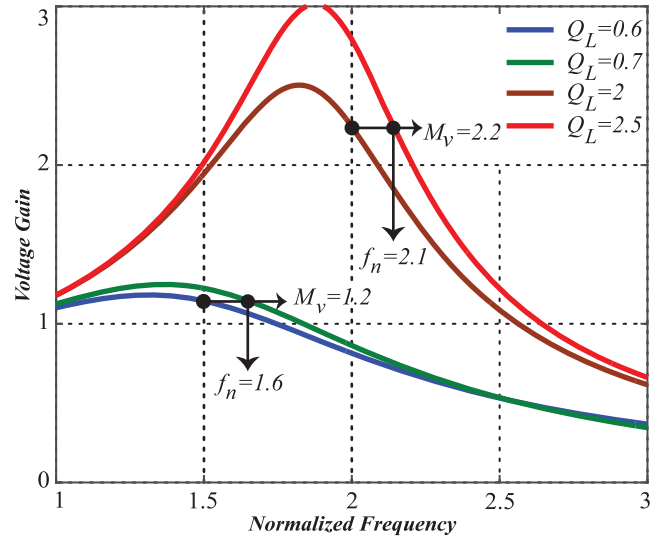

Fig. 10. Magnitude of voltage transfer function (M_v), using the voltage gain equation of the $L3C$ resonant converter for $L_n = 0.25$, and $L_s = 5$, with constant values for normalized load resistances (Q_L).

⑤ and ⑥: When the battery voltage reaches 430 V_{dc}, the battery state of charge enters constant voltage mode. In this stage, the voltage control loop kicks in and regulates the battery voltage at the float voltage by increasing the switching frequency. When the charging current drops to a predefined value (e.g., 3%), the battery charger enters to standby mode.

Fig. 9(c) demonstrates the control block diagram, which is employed for the $L3C$ resonant converter for PV to high voltage battery pack applications. As mentioned, the control scheme consists of the MPPT algorithm and voltage loop, which are responsible for extracting the maximum power from PV panel and regulating the output voltage at the float level, respectively. As mentioned in Section IV, since the resonant circuit provides an inherent short-circuit protection at any operating frequency and limits the maximum output current to 1.5 A, the proposed control scheme does not employ any current loop, neither for the output current regulation, nor for the short-circuit protection.

VI. RESONANT POWER CONVERTER DESIGN

In this section, the design procedure will be presented for power conditioning of a 350-W solar PV panel to high-voltage battery pack, using the proposed $L3C$ resonant converter. The main object during design procedure is to design $L3C$ in such a way as to cover all regions of the power-voltage plane presented in Fig. 1(b) ($V_{\text{pv}} = 24$–45 V_{dc}), while responding to battery different states of charge ($V_{\text{out}} = 230$–430 V_{dc} and $I_{\text{out}} = 0$–1.5 A_{dc}). According to the steady-state analysis of the $L3C$ resonant converter, the voltage gain equation, obtained for $L3C$ steady-state condition, is a function of four normalized variables (L_n, L_s, Q_L, and ω_n). The desired normalized parameters should be selected in such a way to provide essential voltage gain for boosting the voltage from PV panel to high voltage battery while providing soft switching conditions for all semiconductor devices. Fig. 10 presents the voltage transfer function M_v versus normalized frequency for

TABLE I

L3C PROTOTYPE PLATFORM PARAMETERS

Parameters	Value
Input Voltage, V_{in}	$24 - 45VDC$
Output Voltage, $V'_{out,n}$	$230 - 430VDC$
Maximum Output Power, P_{out}	$350W$
Switching Frequency Range, f_s	$180 - 400kHz$
Based Resonant Frequency, f_0	$140kHz$
First Series Resonant Inductance, L_{s_1}	$3.75\mu H$
Second Series Resonant Inductance, L_{s_2}	$0.7\mu H$
Parallel Resonant Inductance, L_p	$15\mu H$
Parallel Resonant Capacitance, C'_p	$5nF$
Transformer Turn's Ratio, $n = \frac{N_p}{N_s}$	$4 : 18$

Fig. 11. Prototype test platform of the *L3C* resonant power converter.

$L_n = 0.25$, $L_s = 5$, and $Q_L = 2$ as the normalized parameters. In this case, $Q_L = 2$ presents the load condition related to the maximum output voltage and output power, $V_{out} = 430$ V_{dc} and $P_{out} = 350$ W at the minimum surface temperature and maximum irradiance (-20 °C and 1000 W/m^2). The main specifications of the battery charger are presented in Table I. According to Table I, the based resonant frequency is equal to $f_0 = 140$ kHz. By choosing $\omega_n = 2$, the switching frequency is calculated as

$$f_0 = 140 \text{ kHz}, \quad f_n = 2, \quad f_n = \frac{f_s}{f_0} \implies f_s = 280 \text{ kHz}. \quad (21)$$

The voltage gain at $f_n = 2$ (brown curve, $Q_L = 2$) for the nominal load conditions are given as follows:

$$M_v = 2.2 \quad \text{for } Q_L = 2, \ L_n = 0.25, \ L_s = 5. \quad (22)$$

Therefore, the parallel resonant capacitor voltage (output voltage) and transformer turns-ratio are calculated as follows:

$$V_{out,n} = M_v.V_{in} = 2.2 * 44.5 = 98\text{V dc}$$
$$n = \frac{N_p}{N_s} = \frac{V_{out,n}}{V'_{out,n}} \implies n = \frac{98}{430} = 0.23. \quad (23)$$

According to (19), the characteristic impedance and resonance frequency are given by:

$$Z_0 = \frac{V_{out}^2}{P_{out} Q_L} = 13.8\Omega, \quad \omega_0 = \frac{\omega_s}{\omega_n} = 280\pi \, e3. \quad (24)$$

Therefore, the resonant components are obtained as follows:

$$L = \frac{Z_0}{\omega_0} = 15.7 \ \mu\text{H}, \quad C_p = \frac{1}{Z_0.\omega_0} = 82 \text{ nF}$$
$$L_{s_1} = 3.75\mu H, \quad L_p = 15 \ \mu H, \quad L_{s_2} = 0.7 \ \mu\text{H}. \quad (25)$$

The *L3C* resonant circuit parameters used in the experimental prototype are summarized in Table I.

VII. EXPERIMENTAL RESULTS AND THEORY VALIDATION

In order to investigate the performance of the proposed fourth-order *L3C* resonant converter, a prototype platform has been employed to extract the maximum obtainable coverage of Fig. 1(b) under different output voltage and current conditions. The test setup picture is presented in Fig. 11. According to Table I, the switching frequency range is between 180 and 350 kHz, and the f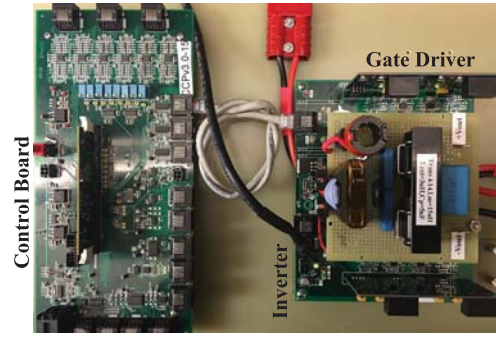requency for maximum output power at maximum output voltage set to be 280 kHz. Due to high-current amplitude in the primary side, a high-efficiency full-bridge inverter with low on-resistance MOSFET (2.5 mOhm) is used to convert the input dc voltage to a high-frequency ac voltage. The resonant tank consists of an external air-core inductor ($L_{\text{ext}} = 3.1$ μH placed in series with the transformer's primary side), an external parallel capacitor (placed in the secondary side of the transformer), and the parasitic components of the transformer (including primary and secondary leakage inductances and magnetizing inductance). In order to investigate the power converter performance, the power platform was tested under different input–output scenarios, and Fig. 12 shows the experimental results for the minimum and maximum output voltage under different input voltage and maximum available power conditions. Each figure contains full-bridge inverter voltage, resonant circuit current, transformer secondary-side voltage, and transformer secondary-side current.

The experimental results show the response of the *L3C* resonant converter to input–output voltage variations, which caused as a result of either changing in the PV panel, or battery state of charge. As mentioned in the introduction, the battery charger must be able to respond to different modes of the charge algorithms and track the input voltage variation in order to transfer the maximum available power. According to the extracted experimental results, the proposed fourth-order *L3C* resonant converter can regulate the output voltage and current over a wide range ($V'_{\text{bat}} = 230$–430 V_{dc} and $I'_{\text{bat}} = 0$–1.5 A_{dc}), and track the input voltage variation in order to extract the maximum available power from PV panel, using the switching frequency modulation. In order to provide soft switching conditions for power MOSFETs, the phase angle of input impedance should be positive. In other words, the input resonant circuit current should remain lagging the full-bridge inverter voltage. According to the experimental results, the zero crossings of the resonant circuit input current are within the inverter output voltage pulse and, as a result, in all of the conditions described, the full-bridge switches are fully turned on under zero voltage. On the other hand, to provide a high-quality output voltage and maximize the converter efficiency, it is vital to realize soft commutation for the output rectifier diodes. Basically, the reverse recovery current of output rectifier diodes during the turn-OFF transition
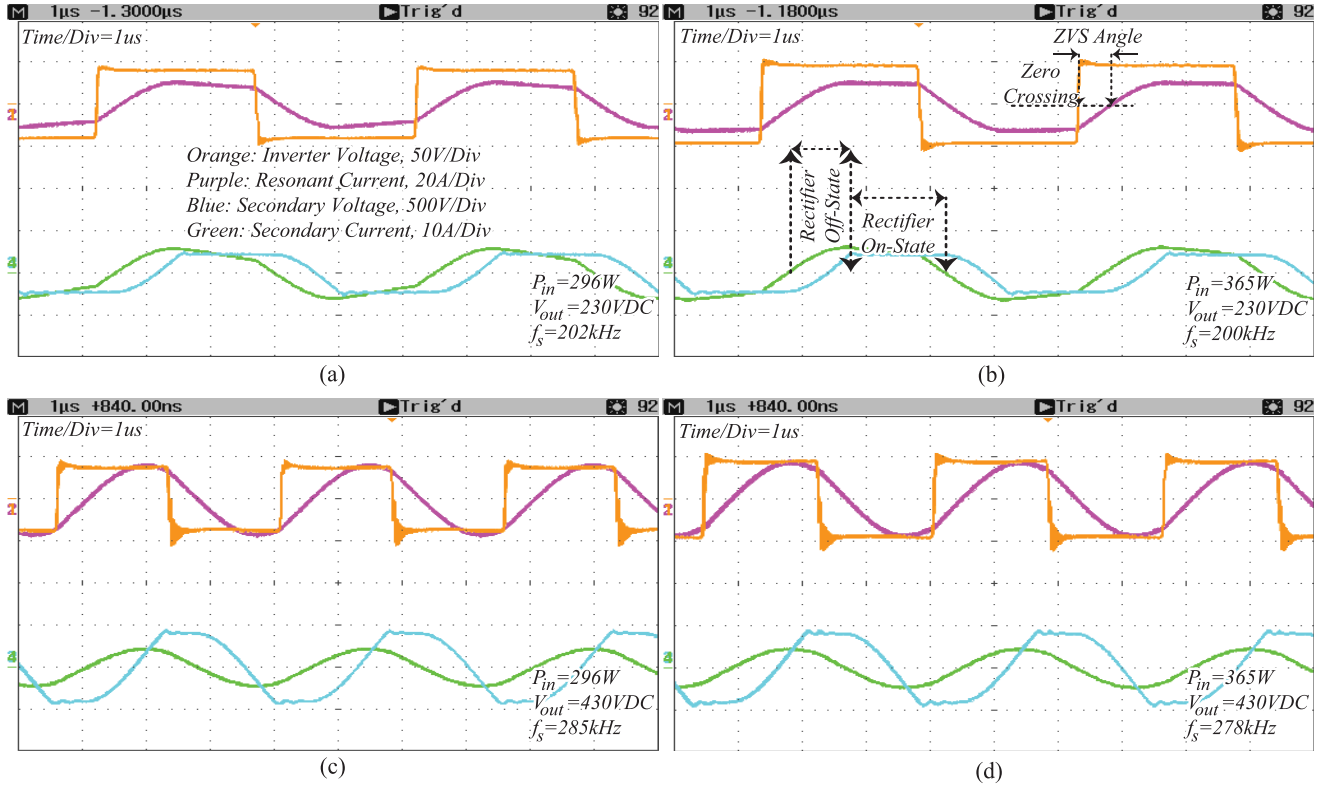
Fig. 12. Experimental results of fourth-order $L3C$ resonant converter platform under different PV panel conditions and minimum-maximum output voltage. (a) 1000 W/m^2 at 25 °C. (b) 1000 W/m^2 at −20 °C. (c) 1000 W/m^2 at 25 °C. (d) 1000 W/m^2 at −20 °C.

leads to high-voltage peak across output diodes and as a result, diodes with more withstand voltage should be selected, which means more conduction losses. Experimental results presented in Fig. 12 include the experimental waveforms of voltage and current on the secondary side of the transformer in the $L3C$ resonant converters. According to Fig. 12, ZCS is provided for output rectifier diodes and voltage peak is eliminated. As indicated in Fig. 12, in the end of power transfer interval, once the transformer secondary current reaches zero, the output diodes current smoothly reaches zero. This causes ZCS at turnOFF and avoids any reverse recovery losses in the output diodes. In addition, the voltage across the diodes is smooth and sinusoidal during the switching transitions which lead to the minimum negative impact of the diode junction capacitance in transient time. As mentioned in Section IV and presented in Fig. 7, there is not any series capacitor in the $L3C$ resonant topology. There is a chance that series capacitor elimination along with nonsimilarity of full-bridge gate signals leads to dc current offset of the resonant current and transformer saturation. However, due to the small air gap of the transformer between its ferrite cores for the magnetizing inductance adjustment, the transformer saturation can be prevented. Experimental results show that in all presented conditions, the resonant current has no dc offset and the transformer operates without any saturation.

Experimental results related to over current and short-circuit conditions demonstrate the ability of the proposed converter in terms of output current limitation during overload conditions. Fig. 13 presents a worst case scenario where the converter
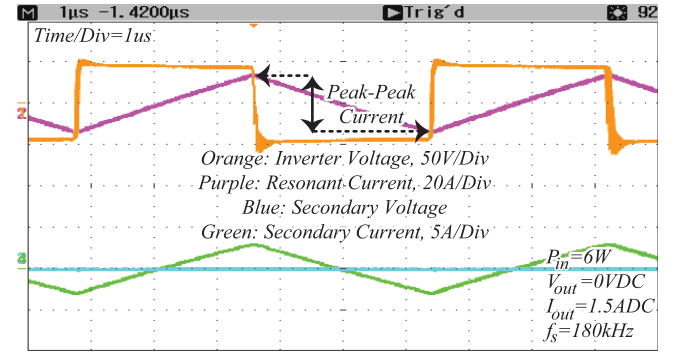

Fig. 13. $L3C$ resonant converter short-circuit test at minimum switching frequency ($f_s = 180$ kHz) and maximum input voltage ($V_{in} = 44$ V$_{dc}$).

operates in output short-circuit and maximum input voltage conditions. According to Fig. 13, the converter can safely work in this situation and limit the output current by $I'_{out} = 1.5$ A$_{dc}$. Fig. 14 presents the efficiency curves for different input PV panel voltages and output battery conditions. Each experimental point in Fig. 14 is related to one maximum power point, presented in Fig. 3. According to these curves, the resonant converters designed for this paper present a maximum efficiency equal to 97.5%. Fig. 14(a) shows the converter efficiency is above 92% from full load to 50% of the load, but due to the circulating current in light load condition, the converter efficiency decreases at light loading conditions.
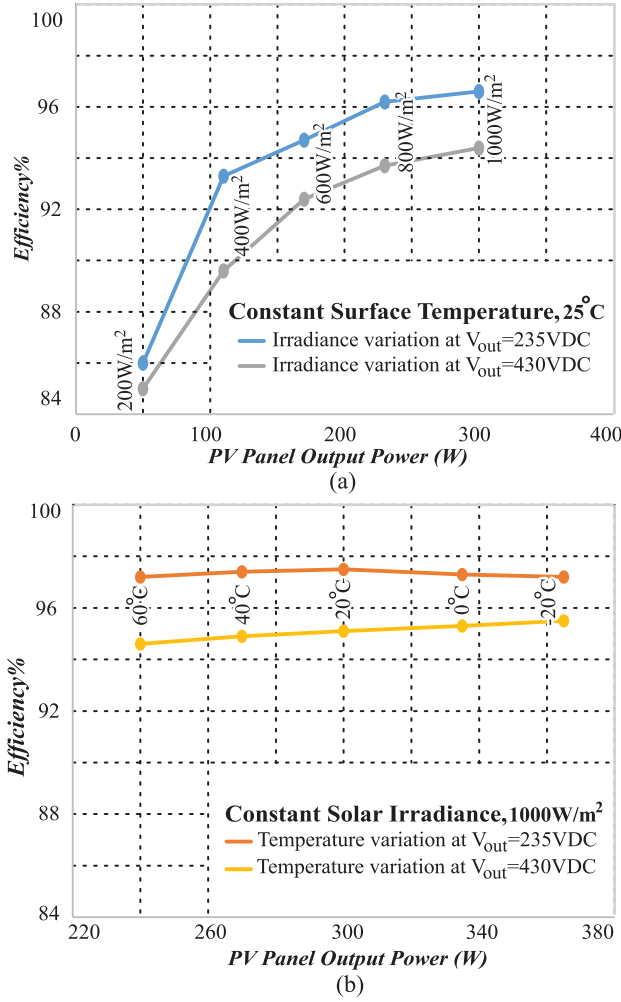
Fig. 14. Efficiency curves of the *L3C* resonant converter for different conditions. (a) Blue and gray lines present efficiency for constant surface temperature (25 °C) and irradiance variations at $V_{out} = 235$ V_{dc} and $V_{out} = 430$ V_{dc}, respectively. (b) Orange and yellow lines present efficiency for constant solar irradiance (1000 W/m^2) and temperature variations at $V_{out} = 235$ V_{dc} and $V_{out} = 430$ V_{dc}, respectively.

VIII. CONCLUSION

This paper introduced the *L3C* resonant power converter with extreme regulation capability, which can be employed for solar battery charger applications. The main advantages of the proposed resonant converter are its ability to respond to different battery states of charge, while tracking the input voltage variations of the PV panel, which occur as a result of changes to the maximum power point. The proposed converter has the voltage gain of more than two, which contributes to the required voltage gain for boosting the input voltage to a high voltage one. Also, the *L3C* topology can provide an inherent over-current protection, which can control the battery current during constant current mode and simplifies the control and protection circuit design. In addition, soft switching of semiconductor devices provides high efficiency and the capability of working in high switching frequency. The complete analysis of the resonant converter along with mathematical equations was presented. The experimental results verify the theoretical analysis and the performance of the

proposed converter in terms of tracking the input voltage for maximum power extraction and operating under different output voltage and current conditions.

REFERENCES

[1] S. A. Arshadi, B. Poorali, E. Adib, and H. Farzanehfard, "High step-up DC–AC inverter suitable for AC module applications," *IEEE Trans. Ind. Electron.*, vol. 63, no. 2, pp. 832–839, Feb. 2016.

[2] R. Ahrabi, H. Ardi, M. Elmi, and A. Ajami, "A novel step-up multi-input DC-DC converter for hybrid electric vehicles application," *IEEE Trans. Power Electron.*, vol. 32, no. 5, pp. 3549–3561, Nov. 2016.

[3] U. R. Prasanna, A. K. Singh, and K. Rajashekara, "Novel bidirectional single-phase single-stage isolated AC–DC converter with PFC for charging of electric vehicles," *IEEE Trans. Transport. Electrific.*, vol. 3, no. 3, pp. 536–544, Sep. 2017.

[4] P. He and A. Khaligh, "Comprehensive analyses and comparison of 1 kW isolated DC-DC converters for bidirectional EV charging systems," *IEEE Trans. Transport. Electrific.*, vol. 3, no. 1, pp. 147–156, Mar. 2017.

[5] VIA Motors Inc. (2014). *SlTRUX Solar Cover for the 2014 VIA VTRUX.* [Online]. Available: www.viamotors.com/vehicles/soltrux

[6] G. Zorpette, "Sun kings cross the outback [solar powered vehicles marathon]," *IEEE Spectr.*, vol. 39, no. 2, pp. 40–46, Feb. 2002.

[7] M. I. Shahzad, S. Iqbal, and S. Taib, "A wide output range HB-2LLC resonant converter with hybrid rectifier for PEV battery charging," *IEEE Trans. Transport. Electrific.*, vol. 3, no. 2, pp. 520–531, Jun. 2017.

[8] F. Musavi, M. Craciun, D. Gautam, W. Eberle, and W. Dunford, "An LLC resonant DC-DC converter for wide output voltage range battery charging applications," *IEEE Trans. Power Electron.*, vol. 28, no. 12, pp. 5437–5445, Dec. 2013.

[9] M. Das and V. Agarwal, "Design and analysis of a high-efficiency DC-DC converter with soft switching capability for renewable energy applications requiring high voltage gain," *IEEE Trans. Ind. Electron.*, vol. 63, no. 5, pp. 2936–2944, May 2016.

[10] L. Müller and J. W. Kimball, "High gain DC–DC converter based on the Cockcroft–Walton multiplier," *IEEE Trans. Power Electron.*, vol. 31, no. 9, pp. 6405–6415, Sep. 2016.

[11] W. Li and X. He, "Review of nonisolated high-step-up DC/DC converters in photovoltaic grid-connected applications," *IEEE Trans. Ind. Electron.*, vol. 58, no. 4, pp. 1239–1250, Apr. 2011.

[12] G. Wu, X. Ruan, and Z. Ye, "Non-isolated high step-up DC-DC converters adopting switched-capacitor cell," *IEEE Trans. Ind. Electron.*, vol. 62, no. 1, pp. 383–393, Jan. 2015.

[13] Y. Tang, D. Fu, T. Wang, and Z. Xu, "Hybrid switched-inductor converters for high step-up conversion," *IEEE Trans. Ind. Electron.*, vol. 62, no. 3, pp. 1480–1490, Mar. 2015.

[14] *UL60950: Safety of Information Technology Equipment*, 3rd ed., Underwrites Lab. Inc., Northbrook, IL, USA, 2000.

[15] *UL1741: Inverters, Converters, Controllers and Interconnection System Equipment for use With Distributed Energy Resources*, Underwrites Lab. Inc., Northbrook, IL, USA, 2010.

[16] M. A. Rezaei, K.-J. Lee, and A. Q. Huang, "A high-efficiency flyback micro-inverter with a new adaptive snubber for photovoltaic applications," *IEEE Trans. Power Electron.*, vol. 31, no. 1, pp. 318–327, Jan. 2016.

[17] Y. Shi, R. Li, Y. Xue, and H. Li, "Optimized operation of current-fed dual active bridge DC-0DC converter for PV applications," *IEEE Trans. Ind. Electron.*, vol. 62, no. 11, pp. 6986–6995, Nov. 2015.

[18] F. Evran and M. Aydemir, "Isolated high step-up DC-DC converter with low voltage stress," *IEEE Trans. Power Electron.*, vol. 29, no. 7, pp. 3591–3603, Jul. 2014.

[19] M. Cacciato, A. Consoli, R. Attanasio, and F. Gennaro, "Soft-switching converter with HF transformer for grid-connected photovoltaic systems," *IEEE Trans. Ind. Electron.*, vol. 57, no. 5, pp. 1678–1686, May 2010.

[20] W. J. Cha, Y. W. Cho, J. M. Kwon, and B. H. Kwon, "Highly efficient microinverter with soft-switching step-up converter and single-switch-modulation inverter," *IEEE Trans. Ind. Electron.*, vol. 62, no. 6, pp. 3516–3523, Jun. 2015.

[21] F. Shang, H. Wu, G. Niu, M. Krishnamurthy, and A. Isurin, "Dynamic analysis and control approach for a high-gain step-up converter for electrified transportation," *IEEE Trans. Transport. Electrific.*, vol. 3, no. 3, pp. 656–667, Sep. 2017.

[22] F. Shang, G. Niu, and M. Krishnamurthy, "Design and analysis of a high-voltage-gain step-up resonant DC–DC converter for transportation applications," *IEEE Trans. Transport. Electrific.*, vol. 3, no. 1, pp. 157–167, Mar. 2017.

[23] Y.-H. Kim, S.-C. Shin, J.-H. Lee, Y.-C. Jung, and C.-Y. Won, "Soft-switching current-fed push–pull converter for 250-W AC module applications," *IEEE Trans. Power Electron.*, vol. 29, no. 2, pp. 863–872, Feb. 2014.

[24] H. Hu, X. Fang, F. Chen, Z. J. Shen, and I. Batarseh, "A modified high-efficiency LLC converter with two transformers for wide input-voltage range applications," *IEEE Trans. Power Electron.*, vol. 28, no. 4, pp. 1946–1960, Apr. 2013.

[25] T. Jiang, J. Zhang, X. Wu, K. Sheng, and Y. Wang, "A bidirectional LLC resonant converter with automatic forward and backward mode transition," *IEEE Trans. Power Electron.*, vol. 30, no. 2, pp. 757–770, Aug. 2014.

[26] N. Shafiei, M. Ordonez, C. Botting, M. Craciun, and M. Edington, "Fourth order L3C resonant converter for wide output voltage regulation," in *Proc. IEEE Appl. Power Electron. Conf. Expo. (APEC)*, Mar. 2015, pp. 1467–1471.

[27] T. LaBella and J.-S. Lai, "A hybrid resonant converter utilizing a bidirectional GaN AC switch for high-efficiency PV applications," *IEEE Trans. Ind. Appl.*, vol. 50, no. 5, pp. 3468–3475, Sep. 2014.

[28] D. Vinnikov, A. Chub, E. Liivik, and I. Roasto, "High-performance quasi-Z-source series resonant DC–DC converter for photovoltaic module-level power electronics applications," *IEEE Trans. Power Electron.*, vol. 32, no. 5, pp. 3634–3650, May 2017.

[29] T. Hongmei, F. MancillaDavid, K. Ellis, and E. Muljadi, "A detailed performance model for photovoltaic systems," Nat. Renew. Energy Lab., Golden, CO, USA, Tech. Rep. NREL/JA-5500-54601, Jul. 2012.

[30] G. M. Masters, *Renewable and Efficient Electric Power Systems*. New York, NY, USA: Wiley, 2004.

[31] A. D. Rajapakse and D. Muthumuni, "Simulation tools for photovoltaic system grid integration studies," in *Proc. IEEE Elect. Power Energy Conf. (EPEC)*, Oct. 2009, pp. 1–5.

[32] S. Kim, J. Jeon, C. Cho, E. Kim, and J. Ahn, "Modeling and simulation of a grid-connected PV generation system for electromagnetic transient analysis," *Solar Energy*, vol. 83, no. 5, pp. 664–678, May 2009.

[33] Canadian Solar Inc. *MAX POWER CS6X-310P*. Accessed: Feb. 2017. [Online]. Available: http://www.canadiansolar.com/na/solar-panels/maxpower.html

[34] M. K. Kazimierczuk and D. Czarkowski, *Resonant Power Converters*. New York, NY, USA: Wiley, 1995.

[35] N. Shafiei, M. Pahlevaninezhad, H. Farzanehfard, A. Bakhshai, and P. Jain, "Analysis of a fifth-order resonant converter for high-voltage DC power supplies," *IEEE Trans. Power Electron.*, vol. 28, no. 1, pp. 85–100, Jan. 2013.

[36] N. Shafiei and M. Ordonez, "Improving the regulation range of EV battery chargers with L3C2 resonant converters," *IEEE Trans. Power Electron.*, vol. 30, no. 6, pp. 3166–3184, Jun. 2015.

[37] Y. A. Ang, C. M. Bingham, M. P. Foster, D. A. Stone, and D. Howe, "Design oriented analysis of fourth-order LCLC converters with capacitive output filter," *IEE Proc.-Electr. Power Appl.*, vol. 152, no. 2, pp. 310–322, Mar. 2005.

[38] J. Biela, U. Badstuebner, and J. W. Kolar, "Design of a 5-kW, 1-U, 10-kW/dm3 resonant DC–DC converter for telecom applications," *IEEE Trans. Power Electron.*, vol. 24, no. 7, pp. 1701–1710, Jul. 2009.

[39] J. A. Martin-Ramos, A. M. Pernia, J. Diaz, F. Nuno, and J. A. Martinez, "Power supply for a high-voltage application," *IEEE Trans. Power Electron.*, vol. 23, no. 4, pp. 1608–1619, Jul. 2008.

[40] M. A. Saket, N. Shafiei, and M. Ordonez, "LLC converters with planar transformers: Issues and mitigation," *IEEE Trans. Power Electron.*, vol. 32, no. 6, pp. 4524–4542, Jun. 2017.

[41] M. A. Saket, N. Shafiei, M. Craciun, C. Botting, and M. Ordonez, "Low parasitics planar transformer for LLC resonant battery chargers," in *Proc. IEEE Appl. Power Electron. Conf. Expo. (APEC)*, Mar. 2016, pp. 854–858.

[42] N. Shafiei, M. Ordonez, M. Craciun, C. Botting, and M. Edington, "Burst mode elimination in high-power LLC resonant battery charger for electric vehicles," *IEEE Trans. Power Electron.*, vol. 31, no. 2, pp. 1173–1188, Feb. 2016.

[43] H. Choi, "Half-bridge LLC resonant converter design using FSFR-series Fairchild power switch," Rev. 1.0.2 22/10/14, Fairchild Semicond., Aurora, CO, USA, Tech. Rep. AN-4151, 2007.

[44] D. Bortis, G. Ortiz, J. W. Kolar, and J. Biela, "Design procedure for compact pulse transformers with rectangular pulse shape and fast rise times," *IEEE Trans. Dielectr. Electr. Insul.*, vol. 18, no. 4, pp. 1171–1180, Aug. 2011.

[45] B. Lee, M. Kim, C. Kim, K. Park, and G. Moon, "Analysis of LLC resonant converter considering effects of parasitic components," in *Proc. Telecommun. Energy Conf.*, 2009, pp. 1–5.

[46] Z. Fang, T. Cai, S. Duan, and C. Chen, "Optimal design methodology for LLC resonant converter in battery charging applications based on time-weighted average efficiency," *IEEE Trans. Power Electron.*, vol. 30, no. 10, pp. 5469–5483, Oct. 2015.

[47] Z. Fang, T. Cai, S. Duan, and C. Chen, "Design methodology of LLC resonant converters for electric vehicle battery chargers," *IEEE Trans. Veh. Technol.*, vol. 63, no. 4, pp. 1581–1592, May 2014.

[48] M. Pahlevaninezhad, P. Das, J. Drobnik, P. Jain, and A. Bakhshai, "A novel ZVZCS full-ridge DC/DC converter used for electric vehicles," *IEEE Trans. Power Electron.*, vol. 27, no. 6, pp. 2752–2769, Jun. 2012.

[49] *Battery Charging*, Texas Instrum., Dallas, TX, USA, 2011.

Navid Shafiei received the B.S. degree in electrical engineering from Kashan University, Kashan, Iran, the M.S. degree in electrical engineering from Islamic Azad University-NajafAbad Branch, Najafabad, Iran, in 2005 and 2011, respectively, and the Ph.D. degree in electrical engineering from The University of British Columbia, Vancouver, BC, Canada, in 2017.

He was a Technical Designer with the Information and Communication Technology Institute, Isfahan University of Technology, Isfahan, Iran, from 2005 to 2013, where he was involved in the design and implementation of resonant converters. He was a Research Scholar with Delta-Q Technologies, Burnaby, BC, from 2013 to 2016. He is currently with Alpha Technologies Ltd., Burnaby, as a Power Supply Design Engineer. His current research interests include advanced soft-switching methods in power converters, high-frequency Magnetics design and their applications in high-efficiency rectifiers for Telecom applications.

Martin Ordonez (S'02–M'09) was born in Neuquen, Argentina. He received the Ing. degree in electronics engineering from National Technological University, Cordoba, Argentina, in 2003, and the M.Eng. and Ph.D. degrees in electrical engineering from the Memorial University of Newfoundland (MUN), St. John's, NL, Canada, in 2006 and 2009, respectively.

He is currently the Canada Research Chair in power converters for Renewable Energy Systems and an Associate Professor with the Department of Electrical and Computer Engineering, The University of British Columbia, Vancouver, BC, Canada, where he is also the holder of the Fred Kaiser Professorship on Power Conversion and Sustainability. He was an Adjunct Professor with Simon Fraser University, Burnaby, BC, and MUN, where he was also a fellow with the School of Graduate Studies. His industrial experience in power conversion includes research and development at AMETEK Programmable Power, San Diego, CA, USA, Deep-Ing Electronica de Potencia, Rosario, Argentina, and TRV Dispositivos, Cordoba, Argentina. With the support of industrial funds and the Natural Sciences and Engineering Research Council, he has contributed to more than 140 publications and research and development reports.

Dr. Ordonez was a recipient of the David Dunsiger Award for Excellence in the Faculty of Engineering and Applied Science in 2009 and the Chancellors Graduate Award/Birks Graduate Medal in 2006. He is a Guest Editor for the IEEE JOURNAL OF EMERGING AND SELECTED TOPICS IN POWER ELECTRONICS, an Associate Editor of the IEEE TRANSACTIONS ON POWER ELECTRONICS, and the Editor for the IEEE TRANSACTIONS ON SUSTAINABLE ENERGY. He serves on several IEEE committees, and reviews widely for the IEEE/IET journals and international conferences.

Mohammad Ali Saket Tokaldani (S'15) was born in Tehran, Iran. He received the B.Sc. degree in electrical engineering from the Amirkabir University of Technology, Tehran, Iran, in 2009, and the M.Sc. degree in power electronics from the Sharif University of Technology, Tehran, in 2011. He is currently pursuing the Ph.D. degree with The University of British Columbia, Vancouver, BC, Canada.

His current research interests include planar magnetics, conducted electromagnetic interference, resonant converters, wireless power transfer, and high-efficiency and low parasitic integrated magnetic structures for dc–dc converters.

Seyed Ali Arefifar (S'06–M'10–SM'17) was born in Isfahan, Iran. He received the B.Sc. and M.Sc. degrees (with Hons.) in electrical engineering and power systems from the Isfahan University of Technology, Isfahan, Iran, in 2001 and 2004, respectively, and the Ph.D. degree in energy systems from the University of Alberta, Edmonton, AB, Canada, in 2010.

He was an NSERC Visiting Fellow with CanmetENERGY, Natural Resources Canada, Varennes, QC, Canada, from 2011 to 2014. From 2014 to 2016, he was Post-Doctoral Research/Teaching Fellow with the Electrical and Computer Engineering Department, The University of British Columbia, Vancouver, BC, Canada. Since 2016, he has been with the Electronics and Communication Engineering Department, Oakland University, MI, USA, as an Assistant Professor. His current research interests include renewable energies and optimizations in planning and operation of smart grids and microgrids.